Available online at www.sciencedirect.com
ScienceDirect
Journal of Solid State Chemistry 181 (2008) 1087–1102
JOURNAL OF SOLID STATE CHEMISTRY
www.elsevier.com/locate/jssc

Local structure and disorder in crystalline $Pb_9Al_8O_{21}$

Alex C. Hannon[a,*], Emma R. Barney[b], Diane Holland[b], Kevin S. Knight[a]

[a]*ISIS Facility, Rutherford Appleton Laboratory, Chilton, Didcot, Oxon OX11 0QX, UK*
[b]*Department of Physics, University of Warwick, Coventry CV4 7AL, UK*

Received 6 December 2007; received in revised form 1 February 2008; accepted 5 February 2008
Available online 10 March 2008

Abstract

Crystalline $Pb_9Al_8O_{21}$ is a model compound for the structure of non-linear optical glasses containing lone-pair ions, and its structure has been investigated by neutron powder diffraction and total scattering, and ^{27}Al magic angle spinning NMR. Rietveld analysis (space group $Pa\bar{3}$ (No. 205), $a = 13.25221(4)$ Å) shows that some of the Pb and O sites have partial occupancies, due to lead volatilisation during sample preparation, and the non-stoichiometric sample composition is $Pb_{9-\delta}Al_8O_{21-\delta}$ with $\delta = 0.54$. The NMR measurements show evidence for a correlation between the chemical shift and the variance of the bond angles at the aluminium sites. The neutron total correlation function shows that the true average Al–O bond length is 0.8% longer than the apparent bond length determined by Rietveld refinement. The thermal variation in bond length is much smaller than the thermal variation in longer interatomic distances determined by Rietveld refinement. The total correlation function is consistent with an interpretation in which AlO_3 groups with an Al–O bond length of 1.651 Å occur as a result of the oxygen vacancies in the structure. The width of the tetrahedral Al–O peak in the correlation function for the crystal is very similar to that for lead aluminate glass, indicating that the extent of static disorder is very similar in the two phases.

Keywords: Local structure; Disorder; Neutron diffraction; Total scattering; Vacancy; Non-stoichiometric; True bond length; AlO_3 group; ^{27}Al NMR

1. Introduction

Glasses containing lone-pair ions are of potential practical importance, due to their non-linear optical properties. These properties arise as a result of the highly polarizable lone-pair charge for lone-pair ions in highly asymmetric environments, and thus it is important to understand the structure of the glass and the effect of composition on the extension in space of the lone-pair charge. As an example of this, we have used several experimental techniques to study the structure of lead aluminate glasses [1], $PbO–Al_2O_3$, which we found to form a glass over the composition range from 72.5 to 80.0 mol% PbO. Our results show that the aluminium sites are four-coordinated by oxygen, while most or all of the lead ions are on asymmetric sites, coordinated by three oxygens in a trigonal pyramid arrangement. More generally, there has been a recent increase in interest in the structure of aluminate glasses [2] and melts [3], arising primarily from recent advances in containerless melting and cooling techniques, which have opened up the accessible range of compositions and conditions.

Often a good model for the local structure in a glass is provided by the structure of a crystal of similar composition. There is a single crystal X-ray diffraction report [4] of the structure of crystalline $Pb_9Al_8O_{21}$ (69.2 mol% PbO) and this is worthy of consideration as a model for the local structure in lead aluminate glasses, with the potential to indicate what types of lead environment may occur in the glass, and what the effect is of the lead ions on the 'host' aluminate network. However, as is shown here, the reported structure of $Pb_9Al_8O_{21}$ has a great deal more disorder in its short-range order (SRO) than is found in the glasses. For this reason a neutron diffraction re-determination of the crystal structure of $Pb_9Al_8O_{21}$ has been performed, and we have used this as an opportunity to investigate the relative amounts of disorder in the SRO of the two phases.

*Corresponding author. Fax: +44 1235 445720.
E-mail address: a.c.hannon@rl.ac.uk (A.C. Hannon).

0022-4596/$ - see front matter © 2008 Elsevier Inc. All rights reserved.
doi:10.1016/j.jssc.2008.02.008

It is well known that crystals possess long-range order (LRO) while glasses do not possess LRO; this is the essential difference between the two types of phase. However, there is little detailed quantitative knowledge of the relative amounts of disorder in the SRO in glasses and crystals (e.g. are the coordination polyhedra in a glass more disordered than in a crystal?). In the work reported here we seek to obtain such knowledge for the lead aluminate system.

2. Theoretical outline

The analysis of the Bragg peaks in the powder diffraction pattern of a crystalline material yields a wealth of information about its average structure. However, there are limitations on its ability to determine how, in a disordered crystal, the local structure deviates from the average structure. The correlation function approach to the analysis of total diffraction data was originally developed mostly for structural studies of non-crystalline materials [5,6]. However, recently correlation function methods are increasingly being applied to the study of the structure of disordered crystalline materials [7–9]. The correlation function provides a measurement of the instantaneous interatomic distances which occur in a sample, and the advantage of using the correlation function method is that it provides a direct measurement of these distances which is model-independent and does not depend on assumptions about the LRO or crystallographic symmetry.

The quantity measured in a neutron diffraction experiment [6,10–12] is the differential scattering cross-section

$$\frac{d\sigma}{d\Omega} = I^S(Q) + i(Q), \tag{1}$$

where $\hbar Q$ is the magnitude of the momentum transfer, $I^S(Q)$ is the self-scattering and $i(Q)$ is the distinct scattering. The self-scattering, which can be calculated approximately, is subtracted from the data to give the distinct scattering. Structural information may then be obtained by a Fourier transformation of $i(Q)$, yielding the total correlation function

$$T'(r) = T^0(r) + \frac{2}{\pi}\int_0^\infty Qi(Q)M(Q)\sin(rQ)\,dQ, \tag{2}$$

where $M(Q)$ is a modification function introduced to take into account the maximum experimentally attainable momentum transfer, Q_{max}, and the prime on $T'(r)$ indicates the real-space broadening, which results from the finite value of Q_{max}. The average density contribution to the total correlation function is

$$T^0(r) = 4\pi r g^0 \left(\sum_l c_l \bar{b}_l\right)^2, \tag{3}$$

where g^0 is the average atomic number density and the l summation is over elements. c_l and $\bar{b}_l$ are, respectively, the atomic fraction and coherent neutron scattering length for element l.

The total correlation function is a weighted sum of partial correlation functions

$$T(r) = \sum_{l,l'} c_l \bar{b}_l \bar{b}_{l'} t_{ll'}(r), \tag{4}$$

where the l and l' summations are each over the elements in the sample. In the harmonic approximation, the contribution to $t_{ll'}(r)$ due to a single interatomic distance, r_{jk}, with a root mean square (RMS) variation in distance of $\left\langle u_{jk}^2 \right\rangle^{1/2}$ is [13]

$$t_{jk}(r) = \frac{n_{jk}}{r_{jk}(2\pi\langle u_{jk}^2\rangle)^{1/2}} \exp\left(-\frac{(r-r_{jk})^2}{2\langle u_{jk}^2\rangle}\right), \tag{5}$$

where n_{jk} is the coordination number of k-type atoms around the origin atom j. The Gaussian in Eq. (5) shows how a peak in the correlation function due to a single well-defined interatomic distance is broadened due to thermal motion. In practice, the observed peaks are further broadened due to the effects of both static disorder and real-space resolution (arising from the finite value of Q_{max}).

3. Experimental

3.1. Sample preparation

A 15 g batch of $Pb_9Al_8O_{21}$ was made by mixing lead (II, IV) oxide (Aldrich) and aluminium oxide (BDH Chemicals Ltd.) powders in the ratio $3Pb_3O_4 \cdot 4Al_2O_3$. The mixture was tumble mixed and pressed into pellets to increase the reaction rate. The pellets were heated to 950 °C at 10 °C/min in an alumina crucible with a loose lid to reduce the loss of lead oxide due to volatilisation. The sample was then cooled immediately to 850 °C, held at this temperature for 72 h, and finally allowed to cool to room temperature in the furnace. The sample was powdered and a conventional X-ray diffraction pattern was taken with Cu$K\alpha$ radiation over an angular range from 5° to 90° to check for phase purity by comparison with the pattern calculated from the literature report of the structure [4]. The density of the powdered sample was measured to be 6.462 g cm^{-3} using a Micromeritics Accupyc 1330 pycnometer with helium as the working fluid. The sample purity was checked by energy-dispersive X-ray fluorescence spectroscopy, using a Panalytical MiniPal 4, and no evidence was found for any impurity elements in the sample.

3.2. ^{27}Al NMR

^{27}Al magic angle spinning (MAS) NMR was conducted at two fields, 14.1 and 8.5 T. At 14.1 T, a Bruker Avance II + 600 spectrometer was used, operating at 156.37 MHz, and with a Bruker 3.2 mm probe with spinning speed 12 kHz. A single pulse programme was used with a 0.5 μs pulse width and 30 s pulse delay. At 8.5 T, a CMX Infinity

360 spectrometer was used, operating at 93.82 MHz, with a Varian 4 mm probe and spinning speed of 10 kHz. A 1 μs pulse width was used with 30 s pulse delay. Chemical shifts were referenced using yttrium aluminium garnet (0.7 ppm with respect to the primary reference $Al(H_2O)_6^{3+}$).

3.3. Neutron powder diffraction

Powder diffraction data were collected for crystalline $Pb_9Al_8O_{21}$ at room temperature using the GEneral Materials neutron diffractometer (GEM) [14], at the ISIS Facility pulsed neutron source. The powder sample was placed inside a 5 mm diameter container made of thin 25 μm vanadium foil so as to minimise the container background and absorption, and neutron diffraction data for this sample were accumulated for about 1 h. Data were also collected for the empty container, an 8.34 mm diameter vanadium rod and the empty diffractometer so that a full set of experimental corrections could be performed using the gudrun programme [15] and the ATLAS software suite [10]. The data used for Rietveld refinement and for extraction of the correlation function were corrected using exactly the same corrections procedure, and this is necessary for the thermal factors from the two analysis methods to be directly comparable. The neutron diffraction data, in both reciprocal- and real-space, are available from the ISIS disordered materials database [16].

4. Results and discussion

4.1. ^{27}Al NMR

The ^{27}Al NMR spectrum, taken at 14.1 T, is shown in Fig. 1, and it indicates that two crystal phases are present in the sample. There is a complex peak at a chemical shift of about 68 ppm, typical of four-coordinated aluminium and similar to the values observed for the aluminium sites in lead aluminate glasses [1]. In the reported structure [4] for $Pb_9Al_8O_{21}$ both aluminium sites are tetrahedral, and hence this peak may be associated with $Pb_9Al_8O_{21}$ as the dominant phase in the sample. The second site is at ~11 ppm, which is a typical position for aluminium atoms which are six-coordinated with oxygen [17]. This suggests that there may be some residual α-Al_2O_3 present (as a result of loss of PbO from the sample), as no six-coordinated aluminium is expected in the crystal structure of $Pb_9Al_8O_{21}$. The integrated intensity of the spectrum, compared with the intensity from a standard sample of α-Al_2O_3, showed that the sample contains 30.5 ± 0.8 mol% Al_2O_3 (close to the expected stoichiometry, 30.8 mol% Al_2O_3, of $Pb_9Al_8O_{21}$). The ratio of intensities of the peaks from the AlO_4 and AlO_6 sites indicates that 8.08 ± 0.02% of the aluminium atoms are six-coordinated, and hence in α-Al_2O_3. The density measurement was corrected for this α-Al_2O_3 content, yielding a value of 6.525 g cm^{-3} for the $Pb_9Al_8O_{21}$ phase.

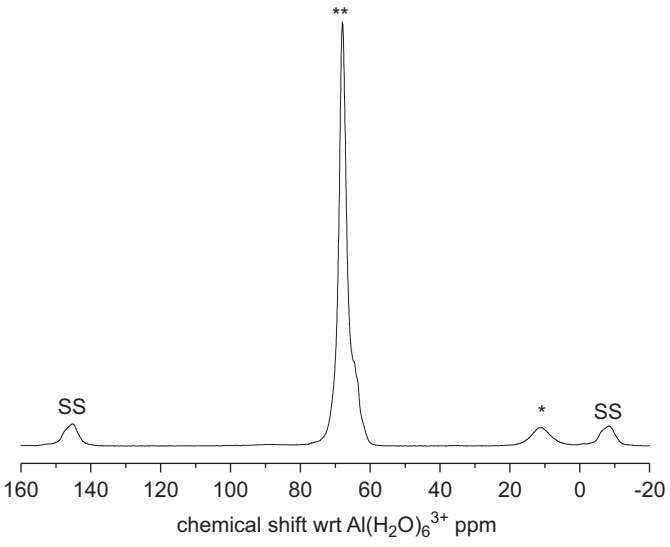

Fig. 1. Horizontal expansion of the ^{27}Al NMR MAS spectrum taken at 14.1 T to show the centrebands from $Pb_9Al_8O_{21}$ (**) and from Al_2O_3 (*), plus the first set of sidebands (SS).

4.2. Rietveld refinement

The original [4] assignment of the space group for $Pb_9Al_8O_{21}$ as $Pa\bar{3}$, on the basis of single crystal X-ray diffraction, was critically examined, by means of a consideration of the long *d*-spacing absences in both our powder X-ray diffraction pattern and the neutron diffraction data from the low angle GEM detector banks, and it was found to be correct. The fully corrected powder neutron diffraction pattern measured by Bank5 of GEM (at a mean scattering angle of 91.42°) is shown in Fig. 2. Rietveld refinements of the data were performed using the TF12LS least-squares fitting programme [18], over a range in *d*-spacing from 0.4099 to 2.3912 Å, and the final fit is shown in Fig. 2. The normalised residual for the fit shows evidence of a few small peaks not included in the fit, the most prominent of which has a *d*-spacing of 2.088 Å, and these were identified as arising from a slight impurity of α-Al_2O_3 in the sample, consistent with the ^{27}Al NMR results.

Initially, Rietveld refinement was performed with the occupancies of all sites fixed at one, and this yielded a lattice parameter, *a*, of 13.25212(4) Å, which is consistent with the value of 13.26 Å obtained in the previous single crystal X-ray diffraction study [4]. However, the density for $Pb_9Al_8O_{21}$, calculated from our lattice parameter, is 6.897 g cm^{-3}, and this value is about 6% larger than the experimental density. Furthermore, an unexpectedly large value of 3.1(2) Å^2 was obtained for the isotropic thermal parameter, *B*, of the O3 site (isotropic temperature factors were used for almost all of the Rietveld refinements described here). An attempt to obtain a more satisfactory value of *B* for the O3 site was made by moving this atom off the high symmetry 4(*a*) site, onto six equivalent low

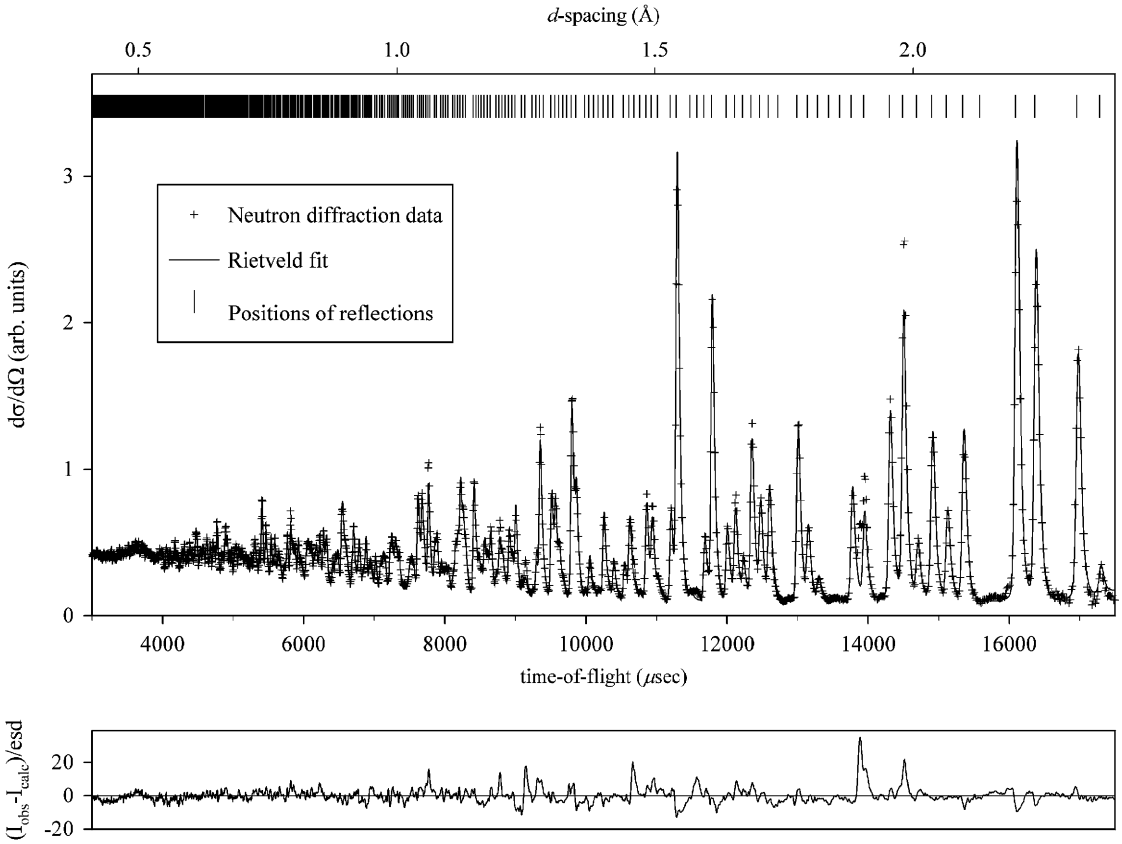

Fig. 2. Final fitted profiles (crosses, observed; line, calculated) from Rietveld refinement for $Pb_9Al_8O_{21}$ shown in upper frame. Vertical tick lines indicate the positions of the allowed reflections. The lower frame shows the residuals $(I_{Iobs}-I_{calc})$/e.s.d. for the fit.

symmetry 24(*d*) sites, each with a partial occupancy of 1/6, but this was unsuccessful because it resulted in Al–O bonds of length 2.72 Å, which is unreasonably long. The O3 site is under-bonded, with a bond angle of 180° (see below), and this suggested that it may have a thermal factor with a significant anisotropy, which could be the reason for the large value obtained for *B*. However, there are several symmetry constraints for the temperature factor of this site [19], and consequently an attempt to perform a refinement with an anisotropic O3 thermal factor yielded a temperature factor which was little changed from the isotropic result.

Since the density calculated for the crystal structure was too high, Rietveld refinement was performed in which the occupancies of the Pb and O sites were allowed to vary. The occupancies of the Pb1, Pb2, O2 and O3 sites were then found to be significantly below one. The occupancies of the other Pb and O sites did not decrease significantly below one, and so these occupancies were fixed at one for the final refinement shown in Fig. 2. (The occupancies of all Al sites were also fixed at one.) The parameters for this final refinement are given in Table 1. The density calculated for these results is $6.553\,g\,cm^{-3}$, which gives much better agreement with the experimental density than was obtained with all occupancies fixed at one. When the partial occupancies in Table 1 are taken into account, the composition of the refined crystal phase is $Pb_{8.49\pm0.07}Al_8O_{20.43\pm0.13}$. Within experimental errors, the reduction in negative charge associated with the O^{2-} sites is balanced by the reduction in positive charge associated with the Pb^{2+} sites (it is assumed that there is no tetravalent Pb), so that the requirement for charge balance is satisfied. The average of the reduction in Pb and O in the formula unit leads to a revised formula for the crystal phase of $Pb_{9-\delta}Al_8O_{21-\delta}$, where $\delta = 0.54$, and this can also be expressed in the form $4(Al_2O_3)\cdot(9-\delta)PbO$, leading to a revised composition for the crystal phase of 67.9 mol% PbO, i.e. for our sample there are 2.16 PbO missing from the unit cell, which contains four formula units. The loss of lead oxide from the crystal structure can be understood as arising from lead volatilisation during sample preparation at high temperature. The lowest occupancy is for the O3 site, and it is notable that, as a result of allowing its occupancy to vary, the thermal factor for this site then has a much more reasonable value than was obtained in the initial refinement.

In summary, the results which were obtained with partial occupancies for some of the atom sites are preferred for three reasons: Firstly, the calculated density is much closer to the measured density; secondly, the reduction in the amount of lead in the chemical formula is charge balanced by the reduction in the amount of oxygen; thirdly, a

Table 1
Unit cell of $Pb_9Al_8O_{21}$ at room temperature; space group $Pa\bar{3}$; $a = 13.25221(4)$ Å; w$R_p = 6.96\%$

Atom	Site	x	y	z	B (Å^2)	Occupancy	Actual number of atoms in unit cell	Number of vacancies in unit cell
Pb1	24(*d*)	0.2658(2)	0.9585(2)	0.3756(2)	0.72(5)	0.92(1)	22.08	1.92
Pb2	4(*b*)	0.5	0.5	0.5	1.24(17)	0.96(3)	3.84	0.16
Pb3	8(*c*)	0.2244(2)	0.2244(2)	0.2244(2)	1.49(9)			
Al1	24(*d*)	0.2163(4)	0.4548(5)	0.1070(4)	0.97(10)			
Al2	8(*c*)	0.0757(5)	0.0757(5)	0.0757(5)	0.87(17)			
O1	24(*d*)	0.0466(3)	0.0503(3)	0.2021(3)	1.12(7)			
O2	24(*d*)	0.7096(3)	0.6214(3)	0.8089(3)	1.15(9)	0.94(2)	22.56	1.44
O3	4(*a*)	0.0	0.0	0.0	1.51(39)	0.76(4)	3.04	0.96
O4	24(*d*)	0.3836(3)	0.4916(3)	0.6697(3)	0.80(7)			
O5	8(*c*)	0.3904(3)	0.3904(3)	0.3904(3)	0.86(12)			

significantly more reasonable thermal parameter is obtained for the O3 site. These three observations together offer strong support for the use of partial occupancies. Hence we conclude that $Pb_9Al_8O_{21}$ is not a line phase occurring at a fixed stoichiometry on the PbO–Al_2O_3 phase diagram [20], but instead that it occurs over a range of compositions, with its exact composition depending on preparation conditions (depending mainly on the volatilisation of lead). The unit cell, shown in Fig. 3, contains 152 atomic sites, of which 147.52 are occupied for our sample. For each site, Table 1 gives the actual number of atoms in the unit cell, and the number of missing atoms. Previously the compound $BaAl_2O_4$ has also been found to be non-stoichiometric [21], with reported compositions covering the range from 44.4 to 50 mol% BaO. It was proposed that reduction in BaO content is accommodated by a small Al–O–Al chain replacing two Ba^{2+} cations. A substitution mechanism of this type could not account for our results concerning the thermal factor and occupancy of the O3 site in $Pb_9Al_8O_{21}$, which are explained in terms of vacancies on the O3 site.

Despite the success of a model with Pb and O vacancies in fitting the powder diffraction data for the crystal, it is less likely that PbO volatilisation will result in vacancies in the structure of lead aluminate glasses, because a glass network has more flexibility than a crystal network to adjust to accommodate a local loss of PbO.

4.3. Bond lengths

The bond lengths in the crystal, d_{jk}, were calculated from the atomic coordinates in Table 1, using the XTAL programme [22,23], and these are given in Table 2, in order of ascending bond length for each origin atom. This programme was also used to evaluate the valences of each of the bonds [24], calculated according to the following expression [25]:

$$v_{jk} = \exp\left(\frac{R_{jk} - d_{jk}}{b}\right), \tag{6}$$

where R_{jk} is the bond-valence parameter for the atom pair (j,k) and b is a constant ($= 0.37$ Å). Values of 1.651 and 2.112 were used for R_{AlO} and R_{PbO}, respectively [26]. The valence sum, $V_j = \sum_k v_{jk}$, over the neighbours (k) of an origin atom (j), should add up to the formal valence of the origin atom (in this case, Pb^{2+}, Al^{3+} or O^{2-}). This requirement can be used to determine the coordination shell for each origin atom by evaluating the running valence sum until a value close to the formal valence is obtained. Table 2 shows the running valence sum for each atomic site, and also the coordination shell determined by this method is indicated by the use of Hoppe's motif of coordination notation [27]. As well as showing whether the coordination polyhedron of an atom has been fully identified, the valence sum can also be useful as a means of judging whether the results of the Rietveld refinement are reasonable. For most of the sites in $Pb_9Al_8O_{21}$, the valence sum values for the complete coordination shell (indicated by bold text in Table 2) show that the valence sum requirement is well satisfied. The valence sums given in Table 2 do not include any attempt to take into account the partial occupancies given in Table 1.

Table 2 also gives the bond lengths and valence sums calculated from the atomic coordinates determined in the previous study [4] of $Pb_9Al_8O_{21}$ (we have used the XTAL programme [22,23] to calculate the bond lengths ourselves, and found that they differ significantly from the values quoted in the original publication). The valence sums for the two aluminium sites differ markedly from the formal valence of three, indicating that the details of the Al–O coordination were not well determined by the previous study. For X-ray diffraction the scattering amplitude of an atom depends on its atomic number ($Z_{Pb} = 82$, $Z_{Al} = 13$, $Z_O = 8$) with the consequence that it is difficult to locate light atoms, especially in the presence of heavy atoms, and this is the probable reason for the imprecise results on the aluminium and oxygen atoms in the previous study. Contrastingly, the aluminium valence sums given in Table 2 for our own results are very close to the ideal value of three. The coherent neutron scattering length

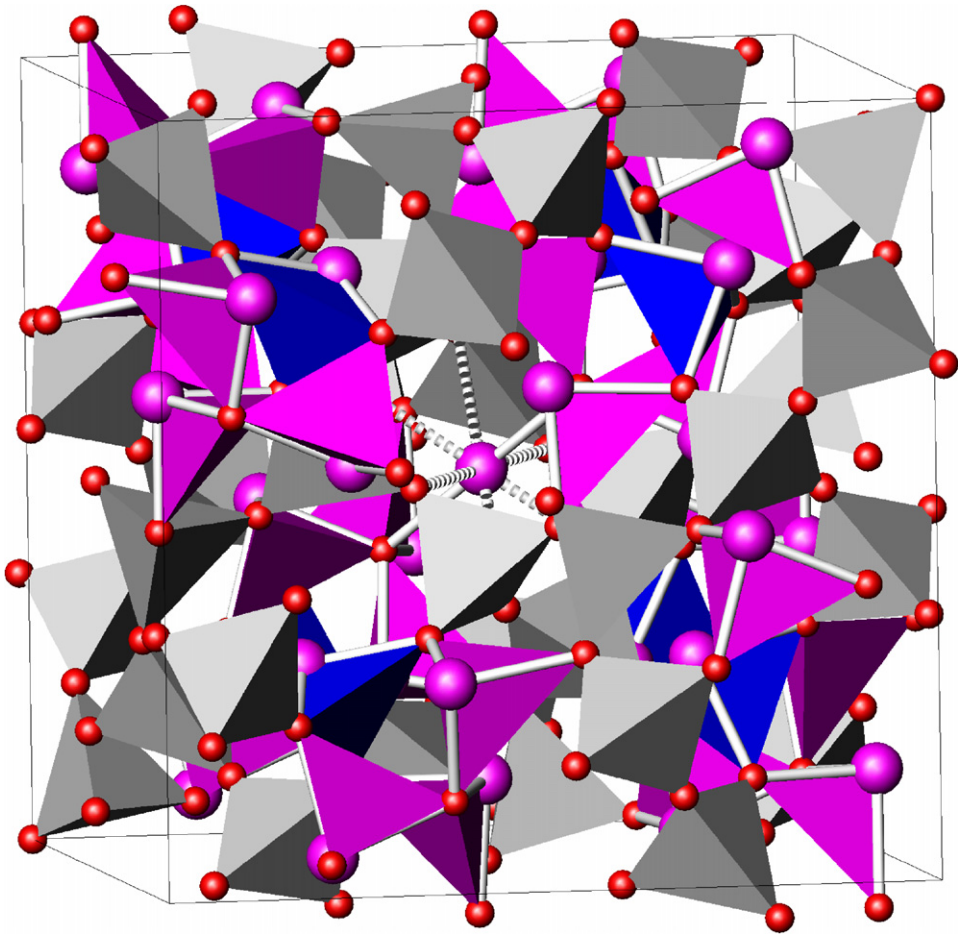

Fig. 3. The unit cell of $Pb_9Al_8O_{21}$. AlO_4 tetrahedra are shown shaded (grey) with (red) spheres at the vertices representing the oxygen atoms. PbO_3 pyramids for the Pb1 and Pb3 sites (defined with a maximum Pb–O bond length of 2.36 Å) are shown shaded (pink for Pb1, and blue for Pb3) with spheres at the vertices representing the lead (pink) and oxygen (red) atoms, and with Pb–O bonds shown along the relevant edges. The Pb2 site at the centre of the cell is shown with continuous short bonds to O5 sites, and dashed long bonds to O4 sites.

varies haphazardly across the period table ($\bar{b}_{Pb} = 9.405$ fm, $\bar{b}_{Al} = 3.449$ fm, $\bar{b}_{O} = 5.803$ fm) [28] so that neutron diffraction is usually much better at locating light atoms in the presence of heavy atoms, and pulsed neutron diffraction has the further advantage of a relatively high resolution in real-space. These two factors explain why better results on the aluminium and oxygen atoms are obtained in the present study. It is also worth noting that the previous report of the structure of $Pb_9Al_8O_{21}$ [4] does not quote thermal factors, and this can be an indication of underlying problems with the analysis, and possibly evidence of disorder in the structure.

Our original motivation for performing structural measurements on crystalline $Pb_9Al_8O_{21}$ was the observation that there is much greater static disorder of the Al–O bond lengths in the previous report of its structure [4] than we have found for lead aluminate glasses [1]. In order to investigate whether our coordinates for Al and O in $Pb_9Al_8O_{21}$ are reasonable, we have compared our results with those for a wide range of aluminate crystal structures, by using Robinson et al.'s method [29] for quantifying the distortion of coordination polyhedra.

For a distorted TO_4 tetrahedron the mean quadratic elongation is defined to be

$$\langle \lambda_{tet} \rangle = \sum_{i=1}^{4} (l_i/l_0)^2/4, \tag{7}$$

where l_i is the length of the bond from the central T atom to the ith oxygen in the distorted tetrahedron, and l_0 is the centre-to-vertex distance for the regular tetrahedron whose volume is equal to that of the distorted tetrahedron. The variance of the angles in the distorted tetrahedron is defined to be

$$\sigma^2_{\theta(tet)} = \sum_{i=1}^{6} (\theta_i - \theta_{tet})^2/5, \tag{8}$$

where θ_{tet} is the $O-\hat{T}-O$ angle for a regular tetrahedron, 109.47°, and θ_i are the $O-\hat{T}-O$ angles in the distorted tetrahedron. Robinson et al. [29] have shown that there is a linear relationship between the mean quadratic elongation, $\langle \lambda_{tet} \rangle$, and the tetrahedral angle variance, $\sigma^2_{\theta(tet)}$.

We have used the XTAL programme [22,23] to calculate $\langle \lambda_{tet} \rangle$ and $\sigma^2_{\theta(tet)}$ for the AlO_4 tetrahedral sites in a number

Table 2
Bond lengths and valences in $Pb_9Al_8O_{21}$

Origin atom	Neighbour	Bond length (Å)	Valence of bond (*e*)	Running valence sum (*e*)	Motif	Bond length from previous study [4] (Å)	Valence sum for previous study (*e*)
Pb1	O5	2.2674	0.657	0.657	PbO_{3+2}	2.29	
	O2*	2.3000	0.602	1.259		2.25	
	O1	2.3554	0.518	1.777		2.40	
	O2*	2.7669	0.170	1.947		2.75	
	O4	3.0160	0.087	**2.034**		2.96	2.048
Pb2	O5 × 2	2.5146	0.337	0.674	PbO_{2+6}	2.43	
	O4 × 6	2.7298	0.188	**1.804**		2.74	1.944
Pb3	O2* × 3	2.2670	0.658	**1.973**	PbO_3	2.26	2.026
Al1	O4	1.7165	0.838	0.838	AlO_4	1.72	
	O4	1.7264	0.816	1.653		1.77	
	O1	1.7920	0.683	2.336		1.87	
	O2*	1.7965	0.675	**3.011**		1.83	2.718
Al2	O3*	1.7371	0.792	0.792	AlO_4	1.72	
	O1 × 3	1.7516	0.762	**3.078**		1.69	3.546
O1	Al1	1.7920	0.683	0.683	OAl_2Pb	1.87	
	Al2	1.7516	0.762	1.445		1.69	
	Pb1*	2.3554	0.518	**1.963**		2.40	1.918
O2	Al1	1.7965	0.675	0.675	$OAlPb_{2+1}$	1.83	
	Pb3	2.2670	0.658	1.333		2.26	
	Pb1*	2.3000	0.602	1.934		2.25	
	Pb1*	2.7669	0.170	**2.105**		2.75	2.151
O3	Al2 × 2	1.7371	0.792	**1.585**	OAl_2	1.72	1.649
O4	Al1	1.7165	0.838	0.838	OAl_2Pb	1.72	
	Al1	1.7264	0.816	1.653		1.77	
	Pb2*	2.7298	0.188	**1.842**		2.74	1.839
O5	Pb1* × 3	2.2674	0.657	1.971	OPb_{3+1}	2.29	
	Pb2*	2.5146	0.337	**2.308**		2.43	2.291

Neighbours with a partial occupancy are indicated by an asterisk.

of aluminate crystal structures from the literature, as shown in Fig. 4. The crystal structures used for this analysis are $CaAl_4O_7$ [30], $Ca_3Al_2O_6$ [31], $Ca_5Al_6O_{14}$ [32], $CaAl_2O_4$ [33], $Na_7Al_3O_8$ [34], $Na_{17}Al_5O_{16}$ [35], $Al_2Ge_2O_7$ [36], $Ca_4Al_6O_{13}$ [37] and $Ca_2Al_2O_5$ [38]. Crystals containing a heavy cation (such as Bi, Ba or Pb) were deliberately excluded because of the possibility that the Al–O coordination has not been determined well due to the difficulty of using X-ray diffraction to locate light atoms in the presence of heavy atoms. The straight line in Fig. 4 is the result of a fit to the data points derived from the structures in the literature (up to a maximum $\sigma^2_{\theta(\mathrm{tet})}$ value of 100), constrained to have a value of one for $\sigma^2_{\theta(\mathrm{tet})} = 0$, yielding $\langle \lambda_{\mathrm{tet}} \rangle = 1 + 0.00026\sigma^2_{\theta(\mathrm{tet})}$. The data points derived from our results (closed squares in Fig. 4) are close to this line, whereas one of the data points (for the Al1 site) derived from the previous report of the structure of $Pb_9Al_8O_{21}$ [4] (open triangles) is unusually far from the line. The fact that the points for $Pb_9Al_8O_{21}$ are on the left-hand side of Fig. 4 indicates that the distortions of the AlO_4 tetrahedra in this crystal are relatively small. The oxygen tetrahedron around the Al1 site is more distorted than for the Al2 site, as indicated by the arrows in Fig. 4.

4.4. ^{27}Al NMR chemical shifts

The centreband of the ^{27}Al NMR spectrum shown in Fig. 1, arising from the $Pb_9Al_8O_{21}$ phase, consists of two peaks, the larger of the two being relatively broad and featureless whilst the smaller has visible quadrupole lineshape. The former is assigned to the more common and more distorted Al1 site and the latter to the Al2 site.

Fig. 5 shows the fits to the ^{27}Al NMR spectra taken at both 14.1 and 8.5 T [38]. The use of two fields reduces the ambiguity of fitting quadrupole lineshapes. Two sites are present, and the parameters from the fit are given in Table 3. The relative intensities of the two peaks in the centreband are 4.1:1. Under MAS, there is loss of central $(\frac{1}{2}, -\frac{1}{2})$ transition intensity from the centreband into the spinning sidebands. The extent of this depends on the quadrupole interaction and therefore is slightly different for each site. A procedure for effecting this correction is

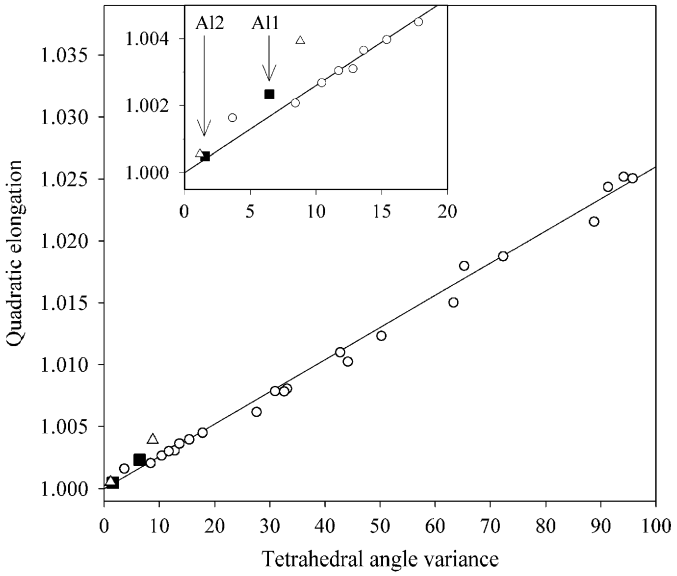

Fig. 4. The mean tetrahedral quadratic elongation plotted against tetrahedral angle variance for AlO_4 tetrahedra in a variety of aluminate crystal structures. Open circles show data derived from crystal structures in the literature, whilst open triangles show the data for the previous study of $Pb_9Al_8O_{21}$ [4], and closed squares show the data for our results on $Pb_9Al_8O_{21}$. The line indicates the linear fit to the data described in the text.

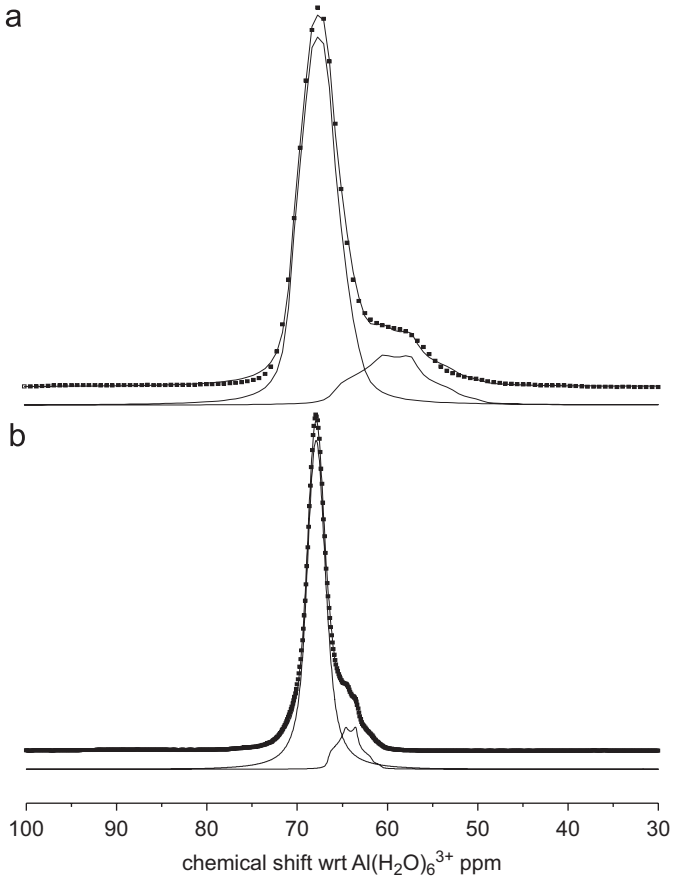

Fig. 5. Two-peak fit to the ^{27}Al NMR centreband, with ν_Q constrained to be 0.314 MHz, for (a) the spectrum obtained at 8.5 T and (b) the spectrum obtained at 14.1 T. The individual contributions from the two sites are offset below the spectra and the overall fits.

Table 3
The parameters from fitting the ^{27}Al NMR spectra taken at both 14.1 and 8.5 T

	Al1	Al2
Isotropic chemical shift (ppm)	69.9±1.0	66.5±0.3
C_Q (MHz)	2.09±0.06	3.04±0.06
η	0.55±0.05	0.60±0.05

given by Massiot et al. [39], which is dependent on the value of $\nu_Q^2/\nu_L\nu_R$, where ν_L is the Larmor frequency, ν_R is the rotation speed and ν_Q is the quadrupole frequency

$$\nu_Q = \frac{3C_Q}{2I(2I-1)}, \tag{9}$$

where C_Q is the quadrupole coupling constant for the Al nucleus in this site and its nuclear spin is $I = 5/2$. The values of ν_Q are sufficiently small for both sites that the correction was negligible, even at the lower field of 8.5 T. The ratio of the two aluminium sites, Al1:Al2, according to the site multiplicity (see Table 1), is 24:8, i.e. 3:1, but this does not agree well with the observation. However, our Rietveld analysis shows that both aluminium sites involve a bond to an oxygen atom with a partial occupancy (either Al1–O2 or Al2–O3—see Tables 1 and 2). Aluminium atoms next to an oxygen vacancy are under-coordinated and, whilst there may be some local reorganisation to offset this, these atoms are likely to have a very distorted environment which may broaden the NMR resonance to an extent which renders it unobservable. We could find no reports in the literature of NMR studies of materials containing AlO_3 units but Tang et al. [40] have obtained ultrawideline ^{27}Al spectra from aluminium which is three-coordinated to carbon or nitrogen. The values of C_Q which they determined are of the order of 30–50 MHz, compared with 2–3 MHz for the tetrahedral coordinations in our sample. This results in lines which would be ~1000 ppm wide under the conditions used in this work and therefore unobservable. If only the Al2 site is unobservable when next to an oxygen vacancy then the predicted intensity ratio is 3.95:1, or if both Al sites are unobservable then the prediction becomes 3.71:1, and both of these values are significantly closer to the experimental value. In addition to this, at both fields, the more intense peak from the Al1 site shows noticeable chemical shift dispersion. This may reflect static disorder in the immediate environment of the Al1 sites and may be related to vacancies on the O2 sites. The lack of an observable ^{27}Al NMR signal for aluminium atoms next to an oxygen vacancy affects the reliability of composition information determined from the NMR intensities in Section 4.1 above. Specifically, it leads to too low an Al_2O_3 content for the overall sample, and too high a value for the amount of α-Al_2O_3 in the sample.

Various empirical relations have been obtained which relate the chemical shift of Al, which is four-coordinated to oxygen, to parameters such as Al–T separation or mean

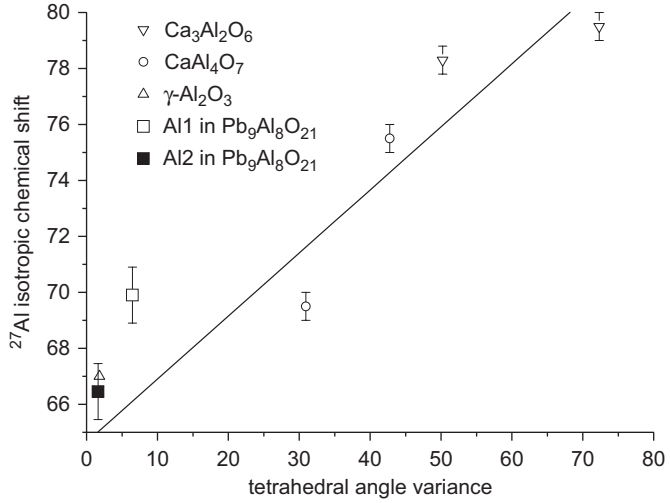

Fig. 6. Isotropic ^{27}Al chemical shift versus tetrahedral angle variance for γ-Al_2O_3 [42], $CaAl_4O_7$ [43], $Ca_3Al_2O_6$ [43] and $Pb_9Al_8O_{21}$ (this work). The straight line is a fit to the literature data.

Al–Ô–T bond angle (e.g. [41]), where T is another framework tetrahedron (Al or Si). These relations work well in these limits but fail in cases like $Pb_9Al_8O_{21}$ where there is significant participation of Pb in the second coordination sphere. It may be possible to overcome these second coordination sphere effects by just examining the AlO_4 tetrahedron and using the parameters derived by Robinson et al. [29] from tetrahedral distortions. There are surprisingly few crystal phases where both accurate atomic coordinates and NMR parameters are available. Fig. 6 shows a plot of isotropic chemical shift versus tetrahedral angle variance for γ-Al_2O_3 [42], $CaAl_4O_7$ [43], $Ca_3Al_2O_6$ [43] and $Pb_9Al_8O_{21}$. There is an approximately linear increase in isotropic shift with distortion of the AlO_4 tetrahedron and the positions of the points for the two sites in $Pb_9Al_8O_{21}$ indicate again that the tetrahedra in this phase are comparatively undistorted. That they are not completely symmetric is evidenced by the finite, though fairly small, values of C_Q for each site.

4.5. Discussion of the structure

Table 4 gives selected bond angle information for the structure of crystalline $Pb_9Al_8O_{21}$, determined by the XTAL programme [22,23]. The $O-\widehat{Al}-O$ bond angles for the four oxygens around each aluminium have narrow distributions which are very close to the ideal tetrahedral bond angle, $\theta_{tet}=\cos^{-1}(-1/3)\approx 109.47^\circ$, and the structure of the crystal involves a network of corner-sharing AlO_4 tetrahedra. For the lone-pair Pb^{2+} ion, a low coordination number (in the range 2–5) involves a highly asymmetric coordination shell in which the bonds to its neighbours are directed throughout only part of the encompassing globe, with an identifiable void in the distribution of bonds [44]. For high coordination numbers (9,10) the coordination shell of Pb^{2+} is symmetric in nature, with the bonds

Table 4
Selected bond angles in $Pb_9Al_8O_{21}$ (the standard deviation of the bond angle distribution is given in brackets where appropriate)

Atoms involved in bond angle	Mean bond angle (deg)
O–Al1–O	109.5 (2.5)
O–Al2–O	109.5 (1.3)
O–Pb1–O in PbO_3 unit	86.5 (6.7)
O5–Pb2–O5	180
O4–Pb2–O4	61.6, 118.4, 180.0
O5–Pb2–O4	82.8, 97.2
O2–Pb3–O2	84.4
Al1–O1–Al2	130.3
Al2–O3–Al2	180.0
Al1–O4–Al1	155.2
Pb–O5–Pb	109.5 (1.0)

distributed much more evenly in direction, whilst for intermediate coordination numbers (6–8) either type of bond distribution may be found. As shown in Fig. 3, the unit cell of the crystal is large, containing 152 atomic sites, and hence Fig. 7 shows the local structure around sites of interest. The Pb3 site in $Pb_9Al_8O_{21}$ involves a PbO_3 trigonal pyramid (see Fig. 7a), which is a very clear example of the asymmetric type of Pb^{2+} coordination. It is notable that the Pb3 site is the only lead site which is fully occupied and that this is the lead site with the strongest bonds, according to the valences in Table 2. The Pb1 site also has the asymmetric type of coordination, with its close neighbours forming a PbO_3 trigonal pyramid (see Fig. 7a), but also two more distant neighbours. Contrastingly, the Pb2 site has the symmetric type of Pb^{2+} coordination, where the directions to the neighbours are distributed much more evenly; the Pb2 site has two axial oxygens at a distance of 2.5146 Å, and also six evenly distributed equatorial oxygens at a distance of 2.7298 Å. A detailed knowledge of these coordination polyhedra is of considerable advantage for understanding the structure of glasses containing lone-pair ions [1]. The O1, O3 and O4 sites are bridging oxygen (BO) sites in which the oxygen acts as a bridge between two corner-sharing AlO_4 tetrahedra (for example, see O3 in Fig. 7b), whilst the O2 site involves a non-bridging oxygen (NBO), which is bonded to only one aluminium. The O5 site is more unusual, in that it involves a non-network oxygen which is tetrahedrally bonded to four lead ions but not to any aluminiums (see Fig. 7b). Previous structural studies of glasses containing lone-pair ions have not considered the possible presence of either symmetric lone-pair ion sites or non-network oxygens [24,45,46], but it must be acknowledged that both of these structural features are very difficult to identify experimentally in a glass.

The O3 site is not adjacent to any of the Pb sites in the crystal structure, and hence it may seem surprising that this site should be subject to the biggest reduction in occupancy. However, two of the structural properties of this site make this large reduction more comprehensible. Firstly, an oxygen on an O3 site is bonded to two

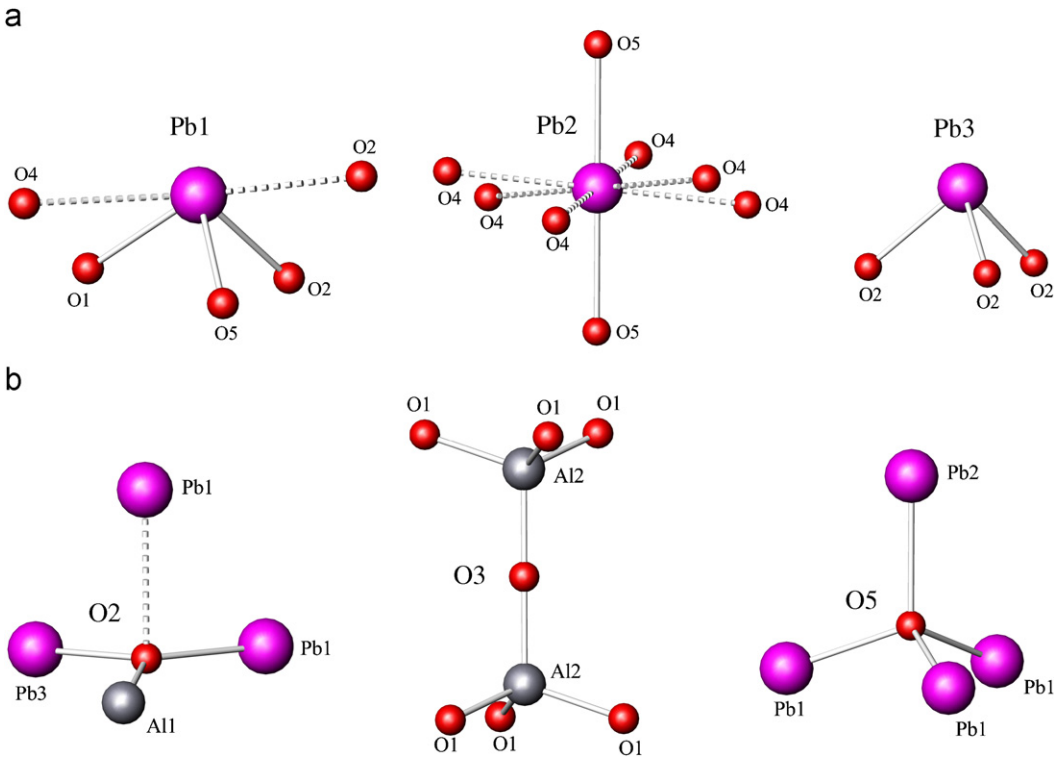

Fig. 7. The local structure around selected sites in $Pb_9Al_8O_{21}$, (a) for the three lead sites (with bonds longer than 2.7 Å shown dashed), and (b) for the O2, O3 and O5 oxygen sites (oxygen atoms are shown as smaller red spheres, whilst cations are shown as larger spheres).

aluminiums with an Al–Ô–Al bond angle of 180°, whereas the preference is normally against straight *M*–O–*M* linkages (where *M* is a cation). Secondly, an O3 oxygen is not bonded to any other atoms besides these two aluminiums, and the bond-valence analysis in Table 2 shows that the O3 site is severely under-bonded. We investigated whether a more reasonable valence sum for the O3 site (i.e. a value close to two) could be obtained by considering interatomic distances longer than the bond lengths shown in Table 2. When distances up to a maximum of 5.0 Å were included, the valence sum only increased a little to 1.704, confirming that an oxygen on the O3 site is significantly under-bonded.

The question arises as to how it is that the Al1 site is more distorted than the Al2 site. For silicate networks it is usual to differentiate between BOs and NBOs, and then to classify the SiO_4 units as Q^n species, where *n* is the number of BOs in the unit [47]. Si–NBO bonds are shorter than Si–BO bonds, and thus a Q^3 is more distorted than a Q^4, because a Q^4 has all bonds the same length, whereas a Q^3 has one shorter bond [48]. In $Pb_9Al_8O_{21}$ the Al1 site is a Q^3, whereas the Al2 site is a Q^4, and thus it might be concluded that the Al1 site is more distorted because it involves a bond to a NBO, whereas Al2 bonds to only BO. However, the bond lengths reported in Table 2 support a different interpretation; the bond to the NBO, Al1–O2, is the longest Al–O bond, at 1.7965 Å. Most of the Al–BO bonds are significantly shorter, in the range ~1.72–1.75 Å, with one exception—the Al1–O1 bond (1.7920 Å), which is almost as long as the Al–NBO bond. In order to gain an understanding of the lengths of the Al–O bonds, a different approach is needed, not based solely on a classification in terms of BO and NBO. Instead, it is useful to consider the Pb–O bonding as an integral part of the network, differentiating the Pb–O bonds into short (~2.3 Å) and long (~2.7 Å) bonds. The O1 site has a long Al–O bond to balance its short bond to Pb1. The O2 site has a long Al–O bond to balance its two short Pb–O bonds. The O3 site has no Pb–O bonds, and hence its Al–O bonds are both short. The O4 site has a long Pb–O bond, but no short Pb–O bonds, and hence both its Al–O bonds are short. In summary, an oxygen site has only short Al–O bonds, unless it has a short Pb–O bond, in which case this is balanced by a long Al–O bond. Thus a description of an aluminate network requires a different approach to silicate networks, with more consideration of the role of the modifier cation (Pb in the case of $Pb_9Al_8O_{21}$).

4.6. Total correlation function

The self-scattering, $I^S(Q)$, was calculated using the Placzek approximation [49], implemented for time-of-flight neutron diffraction [50], and subtracted from the corrected differential scattering cross-section data for each detector bank, according to Eq. (1). Fig. 8 shows the corrected distinct scattering, $i(Q)$, obtained by a combination of data from detector banks 1–5 (at mean scattering angles of 8.99°, 17.26°, 34.22°, 61.83° and 91.42°) on the GEM diffractometer [14], and extrapolated to zero Q using a constant value. The corrections and normalisation for the

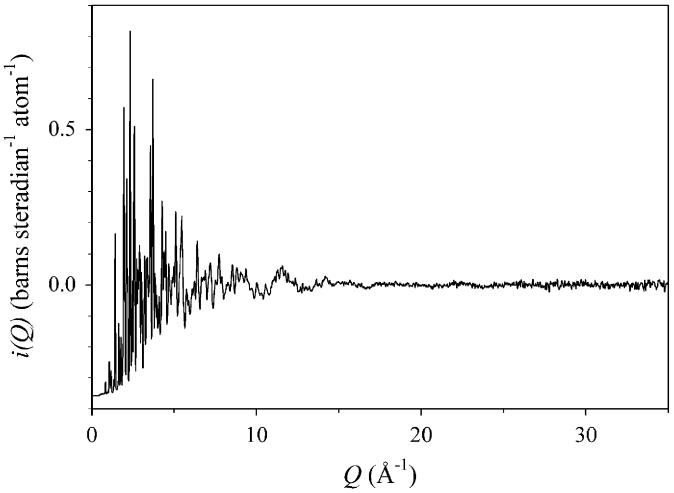

Fig. 8. The distinct scattering, $i(Q)$, for crystalline $Pb_9Al_8O_{21}$.

total diffraction data were evaluated by taking into account the results from Rietveld analysis and ^{27}Al NMR which show that the sample contains two phases, mostly $Pb_{8.46}Al_8O_{20.46}$, but with an impurity phase of α-Al_2O_3. For lower Q, less than about 8 $Å^{-1}$, $i(Q)$ is dominated by sharp Bragg peaks, but at higher Q a more diffuse signal dominates.

Fig. 9 shows the experimental total correlation function, $T_{exp}(r)$, obtained by a Fourier transformation of the distinct scattering for crystalline $Pb_9Al_8O_{21}$, according to Eq. (2), using the Lorch modification function [51] with a maximum momentum transfer, Q_{max}, of 35 $Å^{-1}$. This value for Q_{max} was chosen to be the same as used in the previous neutron diffraction study of glass samples [1] in order to facilitate comparison of the crystal data with the glass data. Fig. 9 also shows the measured correlation function for a glass sample with a composition of 72.5 mol% PbO, which is close to the composition of crystalline $Pb_9Al_8O_{21}$ (69.2 mol% PbO). The first clear peak in the correlation functions at ~1.77 Å arises from Al–O bonds, while the second peak at ~2.29 Å arises from Pb–O bonds. The third peak at ~2.88 Å is predominantly due to O–O distances, but with smaller contributions from other atom pairs, including Pb–O. The correlation functions for the glass and crystal, shown in Fig. 9, are very similar in the region of these first two peaks, but with slightly shorter bonds in the glass. This similarity shows that the crystal provides a good model for the local structure in the glass. The first three correlation function peaks have similar widths for the crystal and the glass, but for longer distances there are greater differences between the crystal and glass correlation functions due to the presence of LRO in only the crystalline phase.

The first two peaks of the correlation function, $T_{exp}(r)$, were fitted using a convolution of the real-space resolution function [10,13] with the peak shape function given by Eqs. (4) and (5). Fig. 10 shows the fitted peaks, and the fit parameters are given in Table 5. The relevant parameters are also given for the glass with 72.5 mol% PbO [1], for

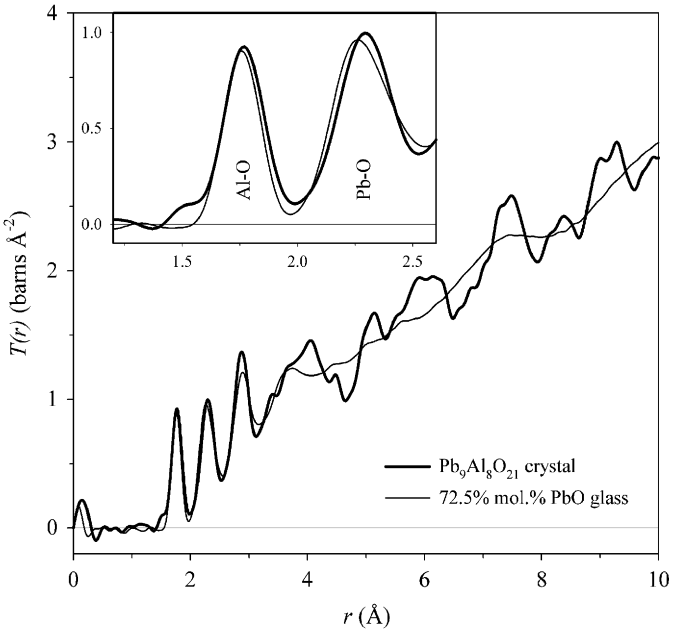

Fig. 9. The measured total correlation function (thick line), $T_{exp}(r)$, for crystalline $Pb_9Al_8O_{21}$, together with the measured total correlation function for a glass [1] with 72.5 mol% PbO (thin line).

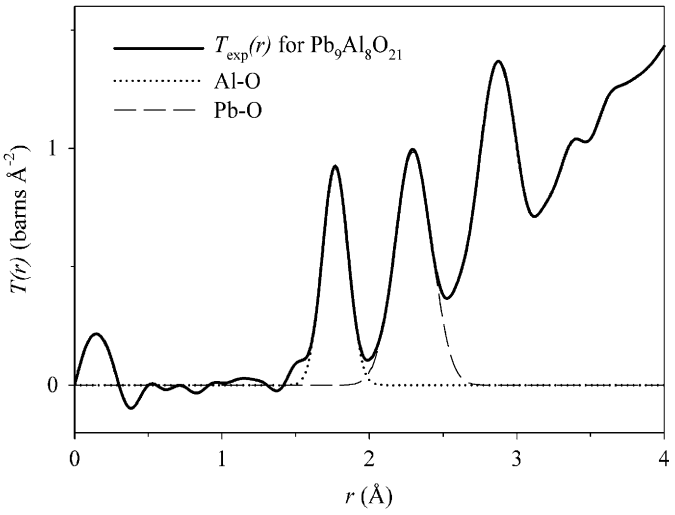

Fig. 10. The measured total correlation function, $T_{exp}(r)$, for crystalline $Pb_9Al_8O_{21}$, together with the results of a fit to the first two peaks. The Al–O component of the fit is shown as a dotted line, whilst the Pb–O component is shown as a dashed line.

comparison. The average Al–O distance from the fit, 1.7698 Å, is ~0.8% longer than the average Al–O bond length, 1.7551 Å, calculated from the Rietveld-derived distances in Table 2 and the oxygen partial occupancies in Table 1. A calculation of the distance between two atoms from Rietveld-derived coordinates yields the distance between the average positions of the two atoms concerned, and as such this is an apparent interatomic distance (or bond length). This is to be contrasted with a correlation function analysis which yields the average instantaneous distance between two atoms, and this is the true interatomic distance. The apparent bond length is always

Table 5
Parameters for the Al–O and Pb–O distributions

	Al–O	Pb–O
r_{jk} for fit to $T_{exp}(r)$ for $Pb_9Al_8O_{21}$ (Å)	1.7698(5)	2.299(1)
$\langle u^2_{jk}\rangle^{1/2}$ for fit to $T_{exp}(r)$ for $Pb_9Al_8O_{21}$ (Å)	0.0684(7)	0.113(1)
r_{jk} for 72.5 mol% PbO glass [1] (Å)	1.7532(5)	2.260(3)
$\langle u^2_{jk}\rangle^{1/2}$ for 72.5 mol% PbO glass [1] (Å)	0.0554(7)	0.098(1)
Calculated $\langle u^2_{jk,static}\rangle^{1/2}$ for $Pb_9Al_8O_{21}$ (Å)	0.0332	0.0372
Calculated $\langle u^2_{jk,static}\rangle^{1/2}$ for Al1–O in $Pb_9Al_8O_{21}$ (Å)	0.0377	–
Calculated $\langle u^2_{jk,static}\rangle^{1/2}$ for Al2–O in $Pb_9Al_8O_{21}$ (Å)	0.0080	–
Calculated $\langle u^2_{jk,thermal}\rangle^{1/2}$ for $Pb_9Al_8O_{21}$ (Å)	0.0598	0.1071
Corrected $\langle u^2_{jk,thermal}\rangle^{1/2}$ for $Pb_9Al_8O_{21}$ (Å)	0.046	

Statistical errors from the fit are given in brackets.

shorter than the true bond length, due to the effect of atomic vibrations [52,53]. A similar but larger effect has been observed for the crystal forms of SiO_2. For example, for β-cristobalite [54], the apparent Si–O bond length is ~4% shorter than the true bond length, due to the rotational vibrations of the rigid SiO_4 tetrahedra. It is likely that the difference in Al–O bond lengths observed here arises in a similar way from the rotational motions of the AlO_4 tetrahedra. This kind of vibrational motion may be associated with low or negative thermal expansion [55].

For the fit shown in Fig. 10, the peak shape function of Eq. (5) was convoluted with the real-space resolution function [13], and hence the fitted peak widths, $\langle u^2_{jk}\rangle^{1/2}$, given in Table 5 include only contributions from static and thermal disorder. Static disorder arises from the variations in distances between the average positions of the atoms, whereas thermal disorder arises from the vibrational motions of the atoms. The contribution to the peak width due to static disorder, $\langle u^2_{jk,static}\rangle^{1/2}$, can be calculated as the standard deviation of the bond lengths given in Table 2 (taking into account the partial occupancies), leading to the values given in Table 5. For the Pb–O distribution, only bonds shorter than 2.5 Å were considered, since this is the appropriate distance range for the fitted peak (see Fig. 10). The full width of the peak, due to both static and thermal disorder, is given by adding in quadrature the individual widths for these two effects, according to

$$\langle u^2_{jk}\rangle = \langle u^2_{jk,thermal}\rangle + \langle u^2_{jk,static}\rangle. \quad (10)$$

The thermal contribution to the peak width, $\langle u^2_{jk,thermal}\rangle^{1/2}$, given in Table 5, was calculated from the fitted peak width and the calculated static contribution, using Eq. (10).

The RMS variation in interatomic distances due to thermal motion can also be calculated from the isotropic temperature factors, B_j, determined by Rietveld refinement, and given in Table 1, according to the following equation [19]:

$$8\pi^2\langle u^2_{jk}\rangle = B_j + B_k. \quad (11)$$

The average B-factor for each element, weighted by occupancy, was calculated to be as follows: $B_{Pb} = 0.96\,Å^2$, $B_{Al} = 0.95\,Å^2$, $B_O = 1.02\,Å^2$. Eq. (11) then shows that the RMS thermal variation in interatomic distance is 0.16 Å for all atom pairs. This value is much larger than the thermal widths determined from the Al–O and Pb–O peaks in the correlation function, given in Table 5. This large disparity arises because of differences between the two techniques of correlation function analysis of the total diffraction pattern, and Rietveld analysis of Bragg diffraction peaks. The thermal widths, $\langle u^2_{jk,thermal}\rangle^{1/2}$, given in Table 5 are determined from the nearest neighbour peaks in the correlation function, and hence they are appropriate to short interatomic distances between bonded atoms, whereas the thermal widths from Rietveld analysis are averaged over all possible interatomic distances, so that the more numerous longer distances dominate. Due to the effects of correlated atomic motions, a smaller thermal width is involved for shorter distances [56], and this is the reason for the disparity.

4.7. Modelling the total correlation function

Fig. 11 shows a comparison between the experimental correlation function, $T_{exp}(r)$, and simulated correlation functions, $T_{sim}(r)$, based on the previous structural data for $Pb_9Al_8O_{21}$ [4]. The simulated correlation functions were calculated from the underlying interatomic distances indicated by the histogram, and hence the static disorder

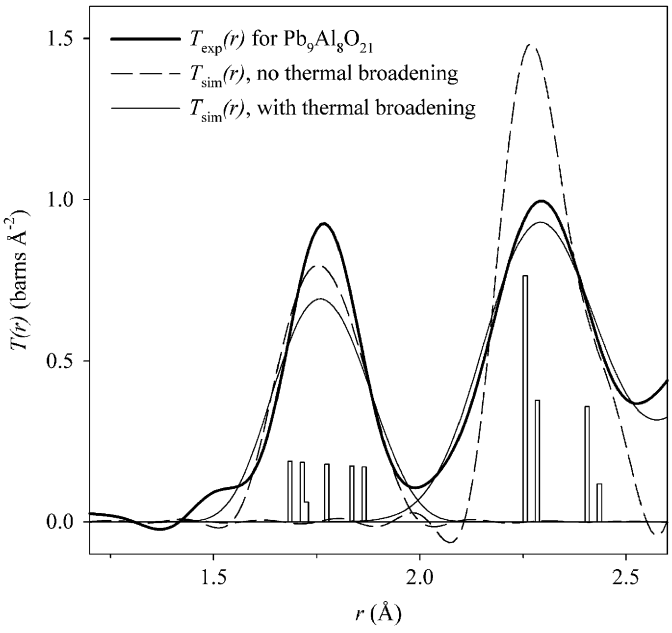

Fig. 11. The measured total correlation function (thick line), $T_{exp}(r)$, for our sample of crystalline $Pb_9Al_8O_{21}$, together with simulated correlation functions, $T_{sim}(r)$, calculated from the interatomic distances (histogram) for the structural results reported by Plötz and Müller-Buschbaum [4]. The dashed line shows a calculation of $T_{sim}(r)$ with resolution broadening only, whilst the thin line shows a calculation of $T_{sim}(r)$ with both resolution and thermal broadening.

of the structure is included in the simulation. In this figure the dashed line shows the Al–O and Pb–O contributions to $T_{sim}(r)$, broadened only for real-space resolution, whilst the thin line shows these contributions after broadening also for the effects of thermal motion, using the thermal widths given in Table 5. For the Pb–O peak, the simulation with only resolution broadening is much narrower than the experimental correlation function, $T_{exp}(r)$, but the simulation with resolution and thermal broadening is close to the experimental result. The static disorder for the previous crystal structure data [4] is slightly greater than observed. Contrastingly, for the Al–O peak the simulation with only resolution broadening is already too broad compared to the experimental data, and the agreement is worse when the effect of thermal motion is included. This shows that the previous structural data for $Pb_9Al_8O_{21}$ [4] have too much static disorder in the Al–O distances, and this was our original reason for investigating the structure of this crystal.

Fig. 12 shows experimental data for our sample, $T_{exp}(r)$, together with a simulated correlation function, $T_{sim}(r)$, calculated as follows: First the simulated correlation function of $Pb_9Al_8O_{21}$ was calculated from the data in Table 1, including the partial occupancies, using the XTAL programme [22,23]. For this simulation the data were broadened for the effects of both real-space resolution [6,10] and thermal atomic motion (Eq. (5)). For Al–O and Pb–O distances less than 3.1 Å, the thermal broadening was done using the appropriate thermal widths in Table 5. Similarly, O–O distances less than 3.5 Å were broadened using a RMS variation of 0.10 Å, because these short

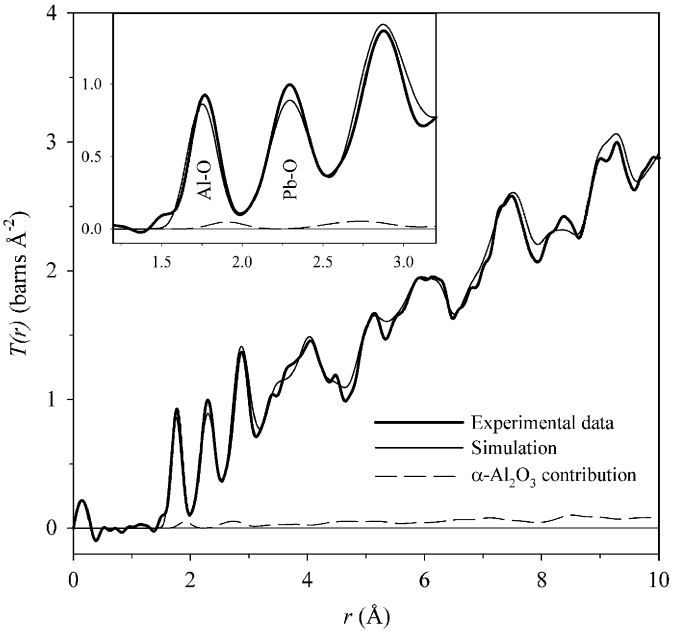

Fig. 12. The measured total correlation function (thick line), $T_{exp}(r)$, for our sample, together with the simulated correlation function (thin line), $T_{sim}(r)$, calculated from our structural data for $Pb_9Al_8O_{21}$ and literature data for α-Al_2O_3 [57]. The dashed line shows the α-Al_2O_3 contribution to $T_{sim}(r)$.

distances occur in relatively rigid coordination polyhedra, and hence are broadened less by atomic motions. For all other interatomic distances (i.e. longer distances), the thermal broadening was done using a thermal width of 0.16 Å, as derived above from the crystallographic *B*-factors. The presence of a second impurity phase in our sample complicates the full simulation of its correlation function. For the formalism used in Eq. (4), the total correlation function of a two-phase sample is given by a weighted sum of the individual phases, provided that correlations between atoms in the two phases are insignificant:

$$T(r) = \frac{N_1}{N_1 + N_2} T_1(r) + \frac{N_2}{N_1 + N_2} T_2(r), \quad (12)$$

where N_i and $T_i(r)$ are, respectively, the number of atoms in phase i and the correlation function for a pure sample of phase i. The correlation function of α-Al_2O_3, corundum, was calculated using the reported lattice parameters and atomic coordinates [57], together with the same thermal widths as used for $Pb_9Al_8O_{21}$. The simulated correlation function for our sample, $T_{sim}(r)$, was then calculated as the weighted sum of the correlation functions of the two individual phases, according to Eq. (12), and using the NMR value for the α-Al_2O_3 content. In Fig. 12 the simulated correlation function is shown as a thin line, whilst the α-Al_2O_3 contribution is shown as a dashed line. The Al–O distance in α-Al_2O_3, in which the coordination is octahedral, occurs at a longer distance than for tetrahedral coordination, as in $Pb_9Al_8O_{21}$ or lead aluminate glasses [1], and the inclusion of the α-Al_2O_3 contribution significantly improves the agreement between $T_{sim}(r)$ and $T_{exp}(r)$ in this region. Nevertheless, the fitted width of the Al–O peak for our sample will be caused to be slightly larger due to the Al–O peak from α-Al_2O_3; the true value for the width of the Al–O peak for $Pb_9Al_8O_{21}$ must be smaller than the value given in Table 5, closer to the peak width for the glass. The Al–O peak in $T_{sim}(r)$ occurs at shorter distance than in $T_{exp}(r)$ because of the difference between apparent and true bond lengths discussed above. The agreement between $T_{sim}(r)$ and $T_{exp}(r)$ at longer distances is good, but not perfect, and differences may arise both because of the difference between true and apparent interatomic distances, and because the transition from short range to long range thermal peak widths is more gradual than in our simulation.

Fig. 13 shows the correlation function, $T_{cor}(r)$, for the $Pb_9Al_8O_{21}$ phase alone; this was obtained by a weighted subtraction of the α-Al_2O_3 contribution from the measured correlation function, $T_{exp}(r)$, according to Eq. (12). $T_{cor}(r)$ was fitted with two peaks, as shown in Fig. 13a, and the fit parameters are given in Table 6. The fitted area of the first peak gives a value of 3.98 ± 0.01 for n_{AlO}, the average number of oxygen atoms about an aluminium atom, while the crystallographic results in Table 1 yield a value of 3.895 for this average Al–O coordination number. The errors quoted in Table 6 are the statistical errors determined in

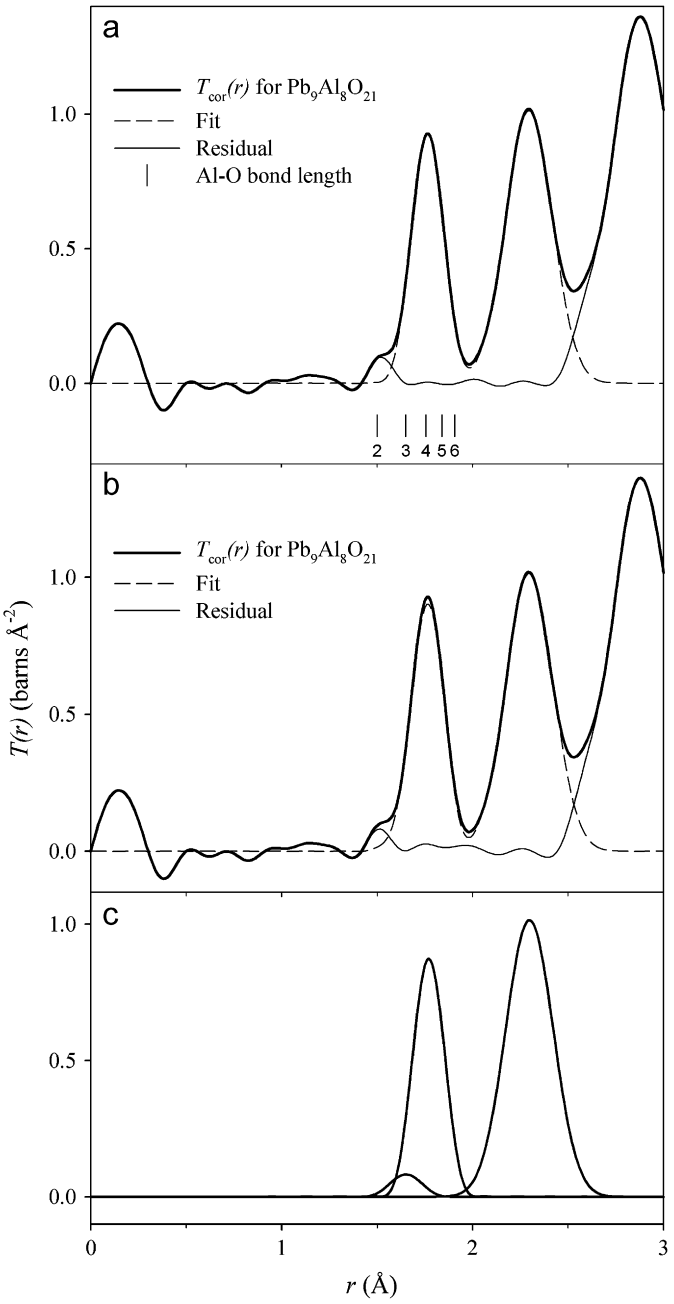

Fig. 13. The corrected correlation function, $T_{cor}(r)$, for $Pb_9Al_8O_{21}$ alone (thick line): (a) together with the results of a two peak fit (showing the fit as a dashed line and the residual as a thin continuous line) and also vertical lines to indicate the bond-valence prediction of bond length for AlO_n groups, (b) together with the results of a constrained three peak fit, and (c) the components of the three peak fit.

Table 6
Parameters for the two-peak fit to $T_{cor}(r)$

	Al–O	Pb–O
r_{jk} (Å)	1.7650(3)	2.2959(3)
$\langle u_{jk}^2 \rangle^{1/2}$ (Å)	0.0630(4)	0.1099(4)
n_{jk}	3.98(1)	2.85(1)

Statistical errors from the fit are given in brackets.

the fit, but there is also a larger systematic contribution to the error on the coordination number. For an ideal case [58], where the sample composition and density are well known, the error on a coordination number from pulsed neutron diffraction may be as low as 1%, but neither of these properties are known with high precision for the current sample. The data quality of an experimental correlation function can be judged from its behaviour at low r before the first real peak [59], and the noise in this region of $T_{cor}(r)$ is relatively large compared to an ideal case [58]. From the magnitude of this low r noise, we estimate a contribution of ± 0.07 to the error on n_{AlO}, due to systematic errors in data normalisation, and conclude that the 2% difference between measured and predicted values is within realistic experimental error.

The prediction of 3.895 for n_{AlO} has two contributions of $n_{AlO}^{IV} = 3.58$ from AlO_4 groups, and $n_{AlO}^{III} = 0.315$ from AlO_3 groups associated with oxygen vacancies in the structure. The question then arises as to how long are Al–O bonds in AlO_3 groups, and where does the AlO_3 contribution occur in the correlation function. Fig. 13 shows that there is a small shoulder on the first peak in $T_{cor}(r)$ at about 1.52 Å, which we have found to be robust to variation in details of data analysis. This shoulder could be assigned to Al–O bonds in AlO_3 groups, since these may be expected to be shorter than in AlO_4 tetrahedra. Little is known about AlO_3 groups, but quantum chemical calculations have been reported [60], in which values of 1.57 and 1.59 Å were predicted for Al–O bond lengths in AlO_3 type environments. However, values averaging 1.66 Å were predicted for Al–O bond lengths in AlO_4 type environments, which is about 0.1 Å shorter than found experimentally (see Table 2), and hence it is more useful to use bond-valence methods to predict the Al–O bond length in AlO_3 groups. If it is assumed that all Al–O bond lengths in an AlO_n group are equal, then the Al–O bond-valence parameter may be used to predict the bond length [61], and the results of these predictions are given in Table 7, and plotted as vertical marks in Fig. 13a. The shoulder at about 1.52 Å is clearly at too short a bond length to be consistent with a three-fold coordination. A three peak fit of $T_{cor}(r)$ was performed, in which the first two components were constrained to have fixed coordination numbers of n_{AlO}^{III} and n_{AlO}^{IV}. Also the first component had a fixed bond length of 1.651 Å (taken from Table 7), and the widths of the first two components were maintained equal. The results of this fit are shown in Fig. 13b, with the individual components of the fit in Fig. 13c, and the parameters of the fit are given in Table 8. The residual for this fit has features of similar

Table 7
Bond-valence prediction of the Al–O bond length for an AlO_n group with equal bond lengths

n_{AlO}	2	3	4	5	6
r_{AlO} (Å)	1.501	1.651	1.757	1.840	1.907

Table 8
Parameters for the constrained three peak fit to $T_{cor}(r)$

	Al–O in AlO_3	Al–O in AlO_4	Pb–O
r_{jk} (Å)	1.651	1.7704(8)	2.298(2)
$\langle u_{jk}^2\rangle^{1/2}$ (Å)	0.057	0.057(1)	0.111(2)
n_{jk}	0.315	3.58	2.9(1)

Statistical errors from the fit are given in brackets.

magnitude to the oscillations in the data at low r before the first peak, showing that this is a reasonable fit and that the data are consistent with an interpretation involving AlO_3 groups with an Al–O bond length of 1.651 Å, as predicted in Table 7. The width of the tetrahedral Al–O peak (due to static and thermal disorder) is 0.057 ± 0.001 Å and this value is very similar to the width of the Al–O peak for the glass (see Table 5), showing that the extent of disorder in Al–O distances in the glass and crystal are very similar. The thermal contribution to the Al–O peak width, $\langle u_{ALO,thermal}^2\rangle^{1/2}$, after correction for the α-Al_2O_3 content and consideration of the effect of AlO_3 groups, was re-calculated using Eq. (10) to be 0.046 ± 0.001 Å, which is larger than the static contribution (see Table 5). If the amplitudes of thermal motion are the same in the crystal and glass, then our results imply that the extent of static disorder in the two phases is the same, so that the AlO_4 coordination polyhedra in the glass are as well defined as in the crystal.

5. Conclusions

Pulsed neutron diffraction has been used to redetermine the structure of crystalline $Pb_9Al_8O_{21}$, and the space group is confirmed to be $Pa\bar{3}$. There is a loss of lead from the sample due to volatilisation during preparation at high temperature, and this leads to both the presence of an α-Al_2O_3 impurity, and to a non-stoichiometric composition for the phase of interest, $Pb_{9-\delta}$ $Al_8O_{21-\delta}$, with $\delta = 0.54$. The loss of PbO is accommodated in the structure by partial occupancies for some of the lead and oxygen sites. ^{27}Al MAS NMR measurements show evidence for the presence of the α-Al_2O_3 impurity, and for the presence of under-coordinated aluminium sites in the crystal. There is also evidence for a correlation between the chemical shift and the variance of the bond angles at the aluminium sites. The neutron total correlation function, obtained by Fourier transformation of the total diffraction, shows that the true average tetrahedral Al–O bond length is 1.7704 ± 0.0008 Å, after corrections, which is about 0.8% longer than the apparent bond length of 1.7551 Å, determined by Rietveld refinement. The crystallographic analysis yields a value of 0.16 Å for the RMS thermal variation in interatomic distances, but the correlation function shows that this value is only appropriate for longer distances, and that the RMS thermal variation in bond lengths is much shorter (0.046 ± 0.001 Å for Al–O bonds). The total correlation function is consistent with an interpretation in which there are AlO_3 groups associated with oxygen vacancies, with an Al–O bond length of 1.651 Å, predicted by a calculation based on the bond-valence parameter. Our results show that crystallographic methods are not able to reveal the extent of the disorder in the SRO, but that this can be obtained from the neutron total correlation function (after a full consideration of all factors). It is then found that the static disorder in the crystal is very similar to that in lead aluminate glass, implying that the AlO_4 coordination polyhedra in the glass are as well defined as in the crystal.

Acknowledgments

This work was funded by EPSRC and the CLRC Centre for Materials Physics and Chemistry, Grant no. CMPC04108.

References

[1] E.R. Barney, A.C. Hannon, D. Holland, S.A. Feller, D. Winslow, R. Biswas, J. Non-Cryst. Solids 353 (2007) 1741.
[2] E.-T. Kang, S.-J. Lee, A.C. Hannon, J. Non-Cryst. Solids 352 (2006) 725.
[3] L. Hennet, I. Pozdnyakova, V. Cristiglio, S. Krishnan, A. Bytchkov, F. Albergamo, G.J. Cuello, J.-F. Brun, H. Fischer, D. Zanghi, S. Brassamin, M.L. Saboungi, D.L. Price, J. Non-Cryst. Solids 353 (2007) 1705.
[4] K.B. Plötz, H. Müller-Buschbaum, Z. Anorg. Allg. Chem. 480 (1981) 149.
[5] B.E. Warren, H. Krutter, O. Morningstar, J. Am. Ceram. Soc. 19 (1936) 202.
[6] A.C. Wright, Adv. Struct. Res. Diffr. Methods 5 (1974) 1.
[7] S.J. Hibble, A.C. Hannon, I.D. Fawcett, J. Phys.: Condens. Matter 11 (1999) 9203.
[8] S.J. Hibble, A.C. Hannon, Local structure: the realm of the chemist?, in: S.J.L. Billinge, M.F. Thorpe (Eds.), From Semiconductors to Proteins: Beyond the Average Structure, Kluwer Academic/Plenum Publishers, New York, 2002, p. 129.
[9] S.J.L. Billinge, M.G. Kanatzidis, Chem. Commun. 1 (2004) 749.
[10] A.C. Hannon, W.S. Howells, A.K. Soper, Inst. Phys. Conf. Ser. 107 (1990) 193.
[11] A.C. Hannon, Neutron diffraction, instrumentation, in: J. Lindon, G. Tranter, J. Holmes (Eds.), Encyclopedia of Spectroscopy and Spectrometry, vol. 2, Academic Press, London, 2000, p. 1479.
[12] A.C. Hannon, Neutron diffraction, theory, in: J. Lindon, G. Tranter, J. Holmes (Eds.), Encyclopedia of Spectroscopy and Spectrometry, vol. 2, Academic Press, London, 2000, p. 1493.
[13] A.C. Hannon, D.I. Grimley, R.A. Hulme, A.C. Wright, R.N. Sinclair, J. Non-Cryst. Solids 177 (1994) 299.
[14] A.C. Hannon, Nucl. Instrum. Methods A 551 (2005) 88.
[15] A.K. Soper, P. Buchanan, 2004, private communication.
[16] A.C. Hannon, ISIS Disordered Materials Database, 2001.
[17] K.J.D. MacKenzie, M.E. Smith, Multinuclear Solid-State Nuclear Magnetic Resonance of Inorganic Materials, Pergamon Press, Oxford, 2002.
[18] W.I.F. David, R.M. Ibberson, J.C. Matthewman, Rutherford Appleton Laboratory Report, RAL-92-032, 1992.
[19] B.T.M. Willis, A.W. Pryor, Thermal Vibrations in Crystallography, Cambridge University Press, Cambridge, 1975.
[20] R.F. Geller, E.N. Bunting, J. Res. Natl. Bur. Stand. 31 (1943) 255.
[21] S.Y. Huang, R. Vondermuhll, J. Ravez, P. Hagenmuller, J. Phys. Chem. Solids 55 (1994) 119.

[22] A.C. Hannon, Rutherford Appleton Laboratory Report, RAL-93-063, 1993.
[23] A.C. Hannon, XTAL correlation function simulation software. 〈http://www.isis.rl.ac.uk/disordered/ACH/Software/XTAL_list.htm〉.
[24] A.C. Hannon, J.M. Parker, Phys. Chem. Glasses 43C (2002) 6.
[25] I.D. Brown, D. Altermatt, Acta Crystallogr. B 41 (1985) 244.
[26] N.E. Brese, M. O'Keeffe, Acta Crystallogr. B 47 (1991) 192.
[27] R. Hoppe, Angew. Chem. Int. Ed. Engl. 19 (1980) 110.
[28] V.F. Sears, Neutron News 3 (1992) 26.
[29] K. Robinson, G.V. Gibbs, P.H. Ribbe, Science 172 (1971) 567.
[30] D.W. Goodwin, A. Lindop, J. Acta Crystallogr. B 26 (1970) 1230.
[31] P. Mondal, J.W. Jeffery, Acta Crystallogr. B 31 (1975) 689.
[32] M.G. Vincent, J.W. Jeffery, Acta Crystallogr. B 34 (1978) 1422.
[33] S. Ito, K. Suzuki, M. Inagaki, S. Naka, Mater. Res. Bull. 15 (1980) 925.
[34] M.G. Barker, P.G. Gadd, M.J. Begley, J. Chem. Soc. Chem. Commun. 1981 (1981) 379.
[35] M.G. Barker, P.G. Gadd, S.C. Wallwork, J. Chem. Soc. Chem. Commun. 1982 (1982) 516.
[36] V. Agafonov, A. Kahn, D. Michel, M. Perez y Jorba, J. Solid State Chem. 62 (1986) 402.
[37] V. Kahlenberg, R.X. Fischer, C.S. Shaw, J. Am. Miner. 85 (2000) 1492.
[38] V. Kahlenberg, R.X. Fischer, C.S. Shaw, J. Am. Mineral. 85 (2000) 1061.
[39] D. Massiot, C. Bessada, J.P. Coutures, F. Taulelle, J. Magn. Res. 90 (1990) 231.
[40] J.A. Tang, J.D. Masuda, T.J. Boyle, R.W. Schurko, Chem. Phys. Chem. 7 (2006) 117.
[41] S.C. Kohn, C.M.B. Henderson, R. Dupree, Am. Mineral. 82 (1997) 1133.
[42] G. Paglia, C.E. Buckley, A.L. Rohl, B.A. Hunter, R.D. Hart, J.V. Hanna, L.T. Byrne, Phys. Rev. B 1 (2003) 68.
[43] J. Skibsted, E. Henderson, H.J. Jakobsen, Inorg. Chem. 32 (1993) 1013.
[44] L. Shimoni-Livny, J.P. Glusker, C.W. Bock, Inorg. Chem. 37 (1998) 1853.
[45] A.C. Hannon, J.M. Parker, B. Vessal, J. Non-Cryst. Solids 196 (1996) 187.
[46] A.C. Hannon, J.M. Parker, B. Vessal, J. Non-Cryst. Solids 232–234 (1998) 51.
[47] R. Dupree, D. Holland, P.W. McMillan, R.F. Pettifer, J. Non-Cryst. Solids 68 (1984) 399.
[48] A.C. Hannon, B. Vessal, J.M. Parker, J. Non-Cryst. Solids 150 (1992) 97.
[49] G. Placzek, Phys. Rev. 86 (1952) 377.
[50] M.A. Howe, R.L. McGreevy, W.S. Howells, J. Phys.: Condens. Matter 1 (1989) 3433.
[51] E. Lorch, J. Phys. C 2 (1969) 229.
[52] W.R. Busing, H.A. Levy, Acta Crystallogr. 17 (1964) 142.
[53] G.D. Barrera, J.A.O. Bruno, T.H.K. Barron, N.L. Allan, J. Phys.: Condens. Matter 17 (2005) R217.
[54] M.T. Dove, D. Keen, A.C. Hannon, I.P. Swainson, Phys. Chem. Miner. 24 (1997) 311.
[55] M.G. Tucker, A.L. Goodwin, M.T. Dove, D.A. Keen, S.A. Wells, J.S.O. Evans, Phys. Rev. Lett. 95 (2005) 255501.
[56] S.J.L. Billinge, Real-space Rietveld: full profile structural refinement of the atomic pair distribution function, in: S.J.L. Billinge, M.F. Thorpe (Eds.), Local Structure from Diffraction, Plenum Press, New York, 1998, p. 137.
[57] H. Graafsma, M. Souhassou, S. Harkema, A. Kvick, C. Lecomte, Acta Crystallogr. B 54 (1998) 193.
[58] A.C. Hannon, D. Di Martino, L.F. Santos, R.M. Almeida, J. Phys. Chem. B 111 (2007) 3342.
[59] A.C. Wright, Neutron and X-ray amorphography, in: C.J. Simmons, O.H. El-Bayoumi (Eds.), Experimental Techniques of Glass Science, American Ceramic Society, Westerville, 1993, p. 205.
[60] A.G. Pelmenshchikov, G.M. Zhidomirov, S. Beran, J. Tino, Phys. Status Solidi A 99 (1987) 57.
[61] A.C. Hannon, J.M. Parker, J. Non-Cryst. Solids 274 (2000) 102.